Journal of Materials Chemistry A

ROYAL SOCIETY OF CHEMISTRY

PAPER

View Article Online
View Journal | View Issue



Cite this: J. Mater. Chem. A, 2025, 13, 34519

# Inducing n-type photoanodic behavior in p-type bismuth ferrite *via* ferroelectric polarization

Michael Gunawan, [a] Yimeng Jin,[a] Teng Chi Leung, [ab] Owen Bowdler,[b] Shujie Zhou,[a] Denny Gunawan, [a] Ming Zhang,[a] Xueqing Fang,[b] Qi Zhang,[bc] Nagarajan Valanoor, [b] Rose Amal, [a] Judy N. Hart, *[b] Jason Scott *[a] and Cui Ying Toe *[ad]

Bismuth ferrite (BFO) has shown great promise as a photoelectrode for photoelectrochemical (PEC) reactions arising from its multiferroic properties at room temperature and suitable band gap for solar harvesting. Further, despite being a p-type semiconductor, the internal electrical field in BFO can induce significant anodic photocurrent, indicating a regulation of the p/n-type behavior of the material by exploiting its switchable polarization capacity. However, the mechanism behind how the polarization field controls the p/n-type behavior of a BFO photoelectrode remains ambiguous. Here, we report on the effects of polarization on surface chemistry, charge dynamics and ultimately PEC performance, and how these effects enable BFO to switch from p-type to n-type behavior. Conventionally, prompting a p-to-n type behavioral switch in BFO requires the introduction of oxygen vacancies by annealing/vacuum treatment at an elevated temperature, where the majority charge carrier in BFO is changed. In contrast, the origin of induced n-type behavior in down-polarized BFO is different and is attributed to a negatively-charged surface, gradient energy modulation, and negatively shifted band energies. The strategy of exploiting the polarization states of BFO photoelectrodes to switch n/p-type behavior offers a facile approach for developing a tunable photoelectrode in PEC systems.

Received 16th June 2025
Accepted 6th August 2025

DOI: 10.1039/d5ta04859a

rsc.li/materials-a



## 1 Introduction

Sunlight-driven water splitting for hydrogen production using a photoelectrochemical (PEC) approach has received significant attention from the global research community.[1,2] Bismuth ferrite ($BiFeO_3$, BFO) stands out as an attractive photoelectrode candidate due to its: (i) narrow band gap ranging from 2.2 to 2.7 eV, which facilitates the absorption of a broad portion of the solar spectrum;[3,4] (ii) non-toxic and lead-free composition; and (iii) suitable conduction band (CB) and valence band (VB) positions for water splitting reactions.[5]

Different from conventional semiconductors, in addition to inherent band-bending at the semiconductor-electrolyte interface (SEI), BFO possesses a ferroelectric polarization-induced internal electric field that can facilitate enhanced charge separation and transport.[6–8] The direction of the internal electrical field can be manipulated by changing the ferroelectric polarization state of BFO.[9] Furthermore, switching the polarization state of BFO alters the electronic state and surface properties of the material, invoking changes in the charge transfer mechanism and surface adsorption behavior.[8,10] For example, an earlier study which integrated BFO with bismuth vanadate (BVO), revealed that the BFO VB and CB energies in the BFO/BVO composites shifted by 0.44 eV between the two polarization states. The difference facilitated control over reaction activity.[11]

BFO naturally exhibits p-type conductivity as it has holes as the majority charge carrier and a Fermi level located close to the VB.[12] When BFO comes into contact with an electrolyte, the Fermi level alignment and charge transfer at the solid electrolyte interface (SEI) invokes a downward band-bending effect which facilitates electron transfer to the SEI.[2] Consequently, BFO is promising as a photocathode in PEC applications.[13,14] In recent years, there has been growing interest in developing n-type BFO for use as a photoanode.[15–17] Similar to other metal oxide semiconductors, BFO can be switched from p-type to n-type by introducing oxygen vacancies. For instance, Radmilovic and co-workers introduced oxygen vacancies in BFO by annealing in a nitrogen environment at 500 °C for 2 hours. The treatment resulted in a negative shift of the flat band potential, bringing the Fermi level closer to the conduction band and converting the BFO from p-type to n-type. In addition, an increase in the charge carrier density was observed, delivering

[a]Particles and Catalysis Research Group, School of Chemical Engineering, UNSW Sydney, NSW, 2052, Australia. E-mail: cuiying.toe@newcastle.edu.au; jason.scott@unsw.edu.au

[b]School of Materials Science and Engineering, UNSW Sydney, NSW 2052, Australia. E-mail: j.hart@unsw.edu.au

[c]CSIRO, Manufacturing, Lindfield, NSW 2070, Australia

[d]School of Engineering, The University of Newcastle, Callaghan, NSW 2308, Australia

an anodic photocurrent density of 400 μA $cm^{-2}$ at 1.23 V *vs.* RHE for sulfite oxidation.[15] An alternative approach involving eight hours of hydrogenation to fabricate oxygen vacancy-rich BFO was reported by Wang and co-workers, which invoked n-type behavior in photoelectrochemical tests.[17] While the above-mentioned approaches have successfully converted p-type BFO into n-type BFO, both methods involve prolonged high temperature annealing in an inert or reducing environment which is time-consuming and energy-intensive. Taking advantage of ferroelectric polarization, BFO has been shown to exhibit a significant anodic photocurrent upon downward polarization compared to the unpoled and upward polarization states.[9,18,19] This unique feature establishes the potential to switch BFO behavior from p-type to n-type-like within seconds at room temperature. Thus, ferroelectric polarization switching offers a promising alternative to time- and energy-intensive heat treatment processes for achieving mild, rapid and potentially reversible n/p-type switching of BFO, but the mechanisms underlying n-type behavior driven by polarization switching and the level of PEC performance that can be achieved in comparison with heat treatment need to be established.

The current work examines the mechanism behind the transition from p-type to n-type behavior associated with ferroelectric polarization switching of BFO in relation to PEC performance. A series of PEC and surface characterization methods, complemented by density functional theory (DFT) calculations, are employed to systematically understand the effects of polarization on surface chemistry, charge dynamics and ultimately PEC performance of polarized BFO. The performance and properties are compared with vacuum-treated BFO as a conventional method of p-to-n type switching. While both approaches introduce oxygen vacancies at the photoelectrode surface, the down-poled BFO photoelectrode gave a higher anodic photocurrent density at 1.23 V *vs.* RHE compared to vacuum-treated BFO. The origin of the higher anodic photocurrent density exhibited by the poling approach relative to vacuum treatment is then discerned. The strategy of exploiting the polarization states of BFO photoelectrodes to switch their p/n-type behavior represents a facile approach to tune photoelectrode properties and performance in a PEC system.

# 2 Experimental

## 2.1 Synthesis of BFO electrode

FTO glass substrates were cleaned by sonication in water, acetone, and ethanol for 15 min in each solvent to remove any surface impurities. The FTO substrates were then dried and treated with UV-ozone cleaner (Ossila, L2002A3) for 15 min before use. The BFO thin film were deposited on FTO according to method developed by Zhang *et al.*[20] BFO precursor solution, with a concentration of 0.25 M, was prepared by initially dissolving bismuth nitrate pentahydrate ($Bi(NO_3)_3 \cdot 5H_2O$) and iron nitrate nonahydrate ($Fe(NO_3)_3 \cdot 9H_2O$) in 2-methoxyethanol (2-MoE) under constant stirring for an hour. The molar ratio of Bi to Fe in the precursor solution was 1 : 1. Acetic anhydride was subsequently added to the solution as a dehydrating and chelating agent under constant stirring for another an hour. The preparation process was performed under ambient atmosphere at room temperature. The precursor solution was deposited on a pre-heated (60 °C) FTO substrate by spin coating at a rate of 4000 rpm for 10 seconds, then dried at 250 °C for 5 min. The deposition-drying cycle was repeated three times. The sample was then subjected to pyrolysis (450 °C, 30 min in air) followed by crystallization (650 °C, 30 min in air). Vacuum annealed samples were prepared following the pyrolysis/crystallization steps. Vacuum annealing involved treating the sample in a Neocera PLD chamber at 300 °C, 0.2 mTorr, for 30 min with a ramp rate of 20 °C $min^{-1}$.

Ferroelectric poling was conducted in a two-electrode electrochemical cell with a BFO film on FTO as the working electrode and a Pt plate as the counter electrode. The poling was carried out in an electrolyte solution consisting of 0.1 M lithium perchlorate ($LiClO_4$) dissolved in propylene carbonate. Propylene carbonate was selected as the solvent due to its wide electrochemical stability window, which prevents solvent oxidation or reduction during the high-voltage poling process.[9] The liquid electrolyte ensures uniform contact with the entire BFO/BVO electrode surface, resulting in consistent and uniform polarization across the sample surface.

## 2.2 BFO thin film characterization

X-ray diffraction (XRD) was used to study the crystal phase/structure using a Philips X'pert MPD-Empyrean using Co Kα radiation at a working potential of 45 kV and a current of 40 mA. A Nova Nano SEM 230 field emission scanning electron microscope (FESEM) was used to characterize the surface morphology and photoelectrocatalyst distribution on the FTO. Transmission electron microscopy (TEM) and selected area electron diffraction (SAED) were conducted on a JEOL JEM-F200 microscope with an accelerating voltage of 200 kV. The surface valence compositions and chemical states were analyzed using X-ray photoelectron spectroscopy (XPS, Thermo ESCALAB 250Xi) with a mono-chromated Al Kα radiation source (1486.68 eV). All binding energy values in the XPS spectra were calibrated using the C 1s peak at 284.8 eV. Commercial scanning probe microscopy (SPM) (Cypher, Asylum Research, US) was used for Kelvin probe force microscopy (KPFM), atomic force microscopy (AFM) and piezoelectric force microscopy (PFM) measurements. UV-vis spectroscopy (Shimadzu UV-3600 UV-vis-NIR spectrophotometer) measurements were conducted over a 350 nm to 800 nm wavelength range with Kubelka–Munk transformation.

Fe K-edge and Bi $L_{III}$-edge X-ray absorption spectra were recorded on the Medium Energy XAS (MEX-1) beamline at the Australian Synchrotron. The beam energy was 3 GeV with a beam current of 200 mA. Data was collected in fluorescence mode. The obtained XAFS data was processed in Athena for background and pre/post-edge line calibration. Fourier transformed fitting was carried out in Artemis. The amplitude reduction factor S02 was defined at 0.78, obtained by the fitting result from standard Fe foil $k^3$-weighted FT-EXAFS spectra. Coordination number, bond length, Debye–Waller factor, and $E_0$ (inner potential correction) shift ($\Delta E_0$) were fitted without being fixed or constrained.

 

### 2.3 Photoelectrochemical performance

PEC performance of the BFO photoelectrodes was determined using a one compartment cell with Ag/AgCl and Pt as the reference and counter electrodes, respectively. The potentials were measured *versus* the Ag/AgCl reference electrode, and were converted to reversible hydrogen electrode (RHE) using the Nernst equation (eqn (1)):

$$E_{RHE} = E_{Ag/AgCl} + E^{0}_{Ag/AgCl} + 0.059\ pH \quad (1)$$

where $E_{RHE}$ refers to the converted potential *vs.* RHE and $E_{Ag/AgCl}$ is the external potential measured against the Ag/AgCl reference electrode. $E^{0}_{Ag/AgCl}$ represents the standard potential of Ag/AgCl, which is equal to 0.197 V at 25 °C.

EIS was conducted under illuminated conditions over the frequency range from 0.01 Hz to $10^5$ Hz. The data was fit by Nova software for the equivalent circuit.

A Newport solar simulator was used as the light source during PEC experiments. The light source was calibrated to AM 1.5 G (100 mW $cm^{-2}$). The electrolyte used during PEC performance assessment was a 0.5 M sodium sulfate solution at neutral pH.

### 2.4 Computational methods

Slab models of BFO and dp-BFO were constructed as described in our previous work.[11] BFO was modelled as up-poled BFO with a $Fe_2O_4$ surface-terminating layer. v-BFO was modelled by introducing surface oxygen vacancies to the up-poled BFO, giving a surface stoichiometry of $Fe_2O_{3.75}$. The dp-BFO was modelled by progressively removing the weakest-bonded surface oxygen atoms from the initial down-poled configuration with $Fe_2O_4$ surface-terminating layer until reaching the energy-minimizing stoichiometry of $Fe_2O_{3.50}$. Density functional theory (DFT) calculations of the three models, *i.e.* BFO, v-BFO and dp-BFO, were done with the CRYSTAL23 code,[21] using the B3LYP method with D3 dispersion corrections and spin polarization.[22–28]

## 3 Results and discussion

### 3.1 Material characteristics

The $BiFeO_3$ photoelectrode fabrication process is illustrated in Fig. 1a. BFO thin films were prepared by spin coating precursor solutions onto a fluorine-doped tin oxide (FTO) glass substrate.[20] The deposited BFO film was heated at 90 °C to induce gelation and then 250 °C to evaporate the solvent. The coating-drying process was repeated three times (unless otherwise stated) to give the desired BFO layer thickness. A BFO photoelectrode was obtained by subjecting the BFO film to pyrolysis and crystallization processes in an air atmosphere at 450 °C and 650 °C, respectively. The as-synthesized BFO film (referred to as pristine BFO) was then polarized using an electrochemical method at ±8 V in a 0.1 M $LiClO_4$ in propylene carbonate electrolyte to control the bulk polarization state. The pristine BFO film was also subjected to vacuum treatment (v-BFO) as a benchmark for the property and performance characteristics.

Scanning electron microscopy (SEM) images (Fig. 1b and c) of the pristine BFO film show polycrystalline BFO covering the FTO substrate, with a thickness of ~135 nm. The X-ray diffraction (XRD) pattern (Fig. 1d) shows that BFO comprises a pure rhombohedral *R*3*c* crystal structure (ICDD: 04-009-2327), dominated by the (012), (104) and (110) orientations at 26.2°, 37.1° and 37.5°, respectively. The bright-field transmission electron microscopy (BF-TEM) image (Fig. 1e) and the corresponding selected area electron diffraction (SAED) pattern (Fig. 1f) further confirm the presence of (012), (110), and (104) oriented BFO with interplanar lattice spacings of 0.402 nm, 0.286 nm, and 0.280 nm, respectively. To confirm the ferroelectric nature of BFO, measurements of the piezoelectric response phase under an applied DC bias were conducted. Notably, an abrupt 180° phase change from −20° to 160° was observed (Fig. 1g) when sweeping the DC voltage. The findings indicate localized switching of the ferroelectric polarization within the BFO thin film.

### 3.2 Photoelectrochemical performance

Photoelectrochemical tests were conducted to observe the PEC behavior of the BFO thin films. PEC linear sweep voltammetry (LSV) tests (Fig. S1, SI) show the pristine BFO photoelectrode exhibits a typical p-type photocurrent density curve with minimal anodic photocurrent density. Cathodic photocurrent refers to the photocurrent density at potentials where the photoelectrode acts as a photocathode, facilitating the hydrogen evolution reaction. In contrast, anodic photocurrent corresponds to the photocurrent density under a positive applied bias, where the photoelectrode operates as a photoanode, driving the oxygen evolution reaction (OER). When polarized with +8 V (referred to as up-BFO), an enhanced cathodic photocurrent density is observed compared to pristine BFO, while the anodic photocurrent density remains unchanged (Fig. S1, SI). Significant enhancement in the anodic photocurrent compared to the pristine BFO are observed when the BFO was poled with −8 V (dp-BFO), accompanied by negligible cathodic photocurrent density (Fig. S1, SI). The behavior suggests a transition of the semiconductor characteristic from p-type to n-type. Accordingly, ensuing physicochemical, electronic, and PEC characterizations focus on the BFO, v-BFO and dp-BFO samples.

The effectiveness of down polarization was evaluated by measuring the PFM phase of the dp-BFO sample (Fig. S2, SI). The resulting phase image reveals a well-oriented PFM phase in the outer region of the scanned area, which is dominated by a yellow contrast. This color signature closely resembles that observed in the central down-poled region that was poled directly by PFM, indicating successful polarization switching toward the downward orientation. The XRD pattern of dp-BFO (Fig. S3, SI) indicates minimum changes on crystallinity of BFO after down-polarization.

The LSV plots (Fig. 2a) show that a cathodic photocurrent density of −40 μA $cm^{-2}$ at 0 V *vs.* RHE and negligible anodic

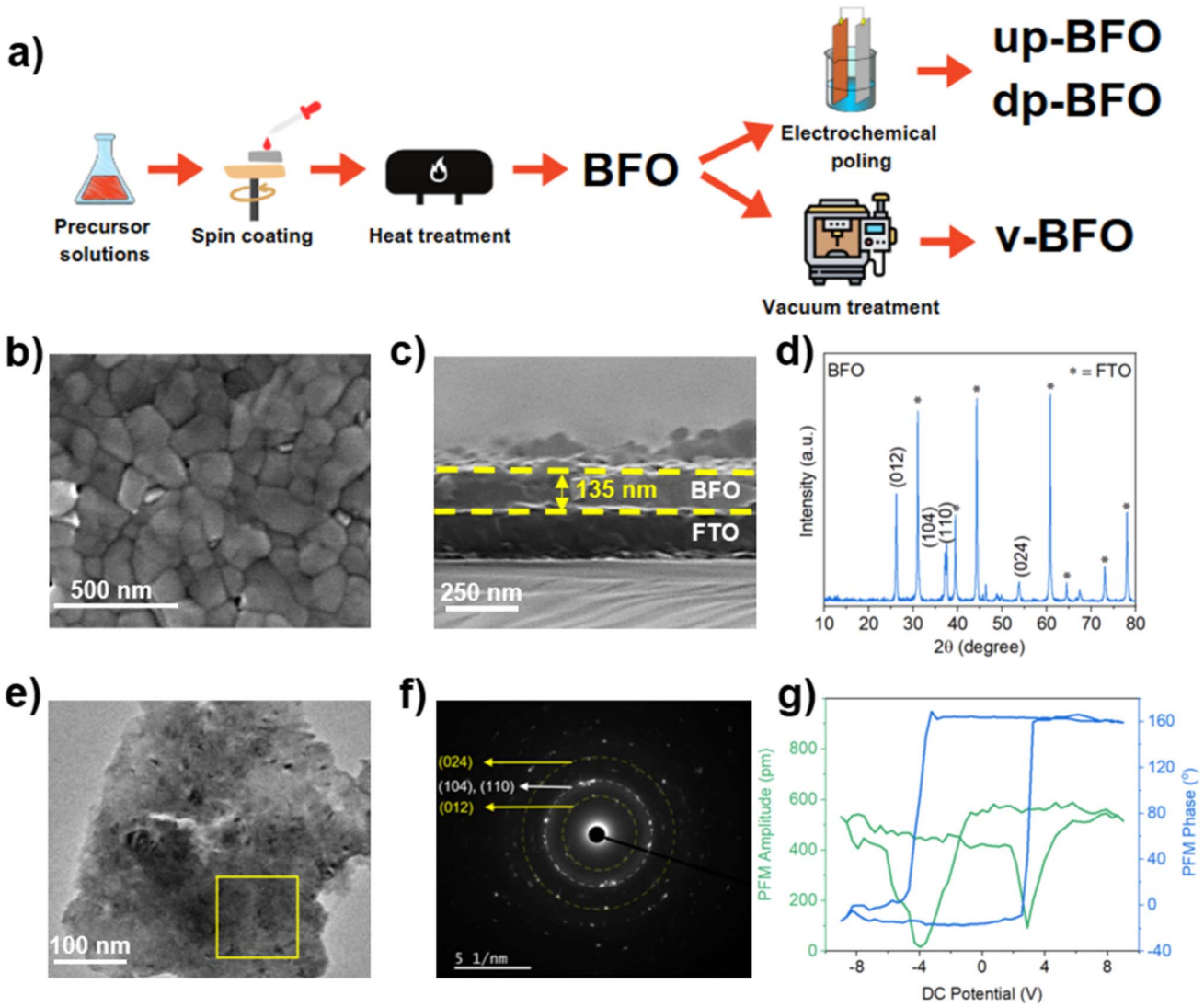


Fig. 1 (a) Schematic depicting the synthesis process for the BFO thin film. (b) Top-view and (c) cross-sectional SEM images of the BFO film. (d) XRD pattern of the BFO sample. (e) Bright-field transmission electron microscopy (BF-TEM) image of the BFO film and (f) selected area electron diffraction (SAED) pattern of the region indicated by the yellow square in (e). (g) PFM amplitude-voltage butterfly loop (green) and phase-voltage hysteresis loop (blue) of the BFO film.

photocurrent density (6 μA $cm^{-2}$) at 1.23 V *vs.* RHE was achieved by the pristine BFO photoelectrode. In contrast, dp-BFO demonstrated an enhanced anodic photocurrent compared to the pristine BFO sample, achieving a photocurrent density of 62 μA $cm^{-2}$ at 1.23 V *vs.* RHE, with a negligible cathodic photocurrent (−1 μA $cm^{-2}$ at 0 V *vs.* RHE). When oxygen vacancies were introduced into the v-BFO, it exhibited an anodic photocurrent density of 25 μA $cm^{-2}$ at 1.23 V *vs.* RHE with a decrease in the cathodic photocurrent density magnitude compared with pristine BFO (−16 μA $cm^{-2}$ at 0 V *vs.* RHE). Similar trends were evident in amperometry measurements of the photoelectrodes at 1.23 V *vs.* RHE (Fig. 2b). They show a significant photocurrent density for both dp-BFO and v-BFO at this positive bias, with the pristine BFO sample offering only a small photocurrent. Conversely, both v-BFO and dp-BFO exhibited lower photocurrent density magnitudes at 0 V *vs.* RHE relative to the pristine BFO (Fig. S4, SI). These trends suggest that both dp-BFO and v-BFO exhibit n-type-like behavior.

The photocurrent density trends at positive applied potentials were also reflected in the Nyquist plots (Fig. 2c) obtained from photoelectrochemical impedance spectroscopy (PEIS) measurements at 1.23 V *vs.* RHE. The obtained plots were fitted to an equivalent circuit, as shown in the Fig. 2c inset, where $R_s$ and $R_p$ represent the charge transfer resistance values of the electrolyte solution and within the photoanode, respectively.[29] The fitting parameters (available in Table S1, SI) indicate that all samples exhibit similar $R_s$ values, which accounts for the resistance of the electrolyte. In contrast, the $R_p$ value decreased from 544 kΩ for the pristine BFO to 178 kΩ for v-BFO, and further to 11.3 kΩ for dp-BFO, suggesting improved photogenerated charge dynamics upon vacuum treatment and downpoling.

 

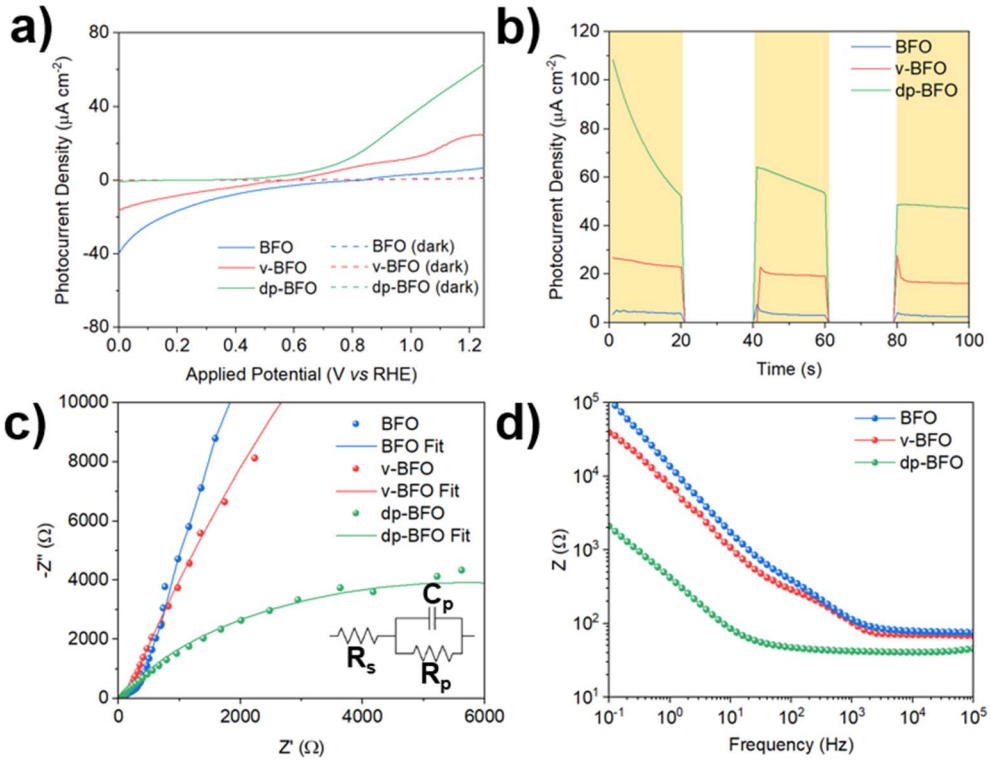


Fig. 2 (a) Linear sweep voltammetry profiles and (b) light-on/light-off chronoamperometry curves, (c) Nyquist plots with inset depicting equivalent circuit employed to calculate the parameters given in Table S1. (SI), and (d) Bode's plots of the BFO-based photoelectrodes measured in 0.5 M sodium sulfate solution under AM 1.5 G, 100 mW $cm^{-2}$ illumination. The chronoamperometry and photoelectrochemical impedance spectroscopy tests were conducted at 1.23 V *vs.* RHE.

Bode's plots were also constructed to identify the key factors behind the improved charge dynamics of the dp-BFO and v-BFO samples. The Bode's plots of the photoelectrodes reflect the impedance ($Z$) of the photoelectrode at various frequencies (Fig. 2d). The lower and higher frequency regions of Bode's plots are typically associated with charge transfer impedance at the SEI and in the bulk photoelectrode, respectively. The v-BFO sample showed a decrease in impedance at lower frequencies, while no significant difference was observed in the higher frequency region. The finding demonstrates that the charge transfer improvement for v-BFO is only observed at the SEI and not within the bulk structure. In contrast, dp-BFO exhibits a decrease in impedance value for both the lower and higher frequency regions, indicating a decrease in both bulk and interfacial charge transfer resistance compared to the pristine BFO.

### 3.3 Spectroscopic analyses

Examination of the surface chemistry and bulk structure of the BFO samples was conducted to identify the effect of vacuum treatment and down polarization on the photoelectrodes. Raman spectroscopy (Fig. 3a) reveals changes in the bonds of both dp-BFO and v-BFO compared to the pristine BFO photoelectrode. At room temperature, $BiFeO_3$ typically presents 13 Raman modes ($4A_1$ + 9E) at low frequencies (up to 262 $cm^{-1}$).[30–33] For both v-BFO and dp-BFO, the $A_1$ peak at 140 $cm^{-1}$ (Fig. 3b) is red-shifted relative to pristine BFO, indicating changes in the Bi–O bonds. Lahmar *et al.* reported that the red-shifted peak at 140 $cm^{-1}$ is induced by surficial oxygen vacancies which affect Bi–O bonds at the surface.[34]

To further elucidate the chemical changes on the photoelectrode surfaces, X-ray photoelectron spectroscopy (XPS) was conducted. As shown in Fig. 3c, the O 1s signal for BFO can be deconvoluted into two peaks at 529.4 and 531.1 eV, attributed to lattice oxygen ($O_L$) and chemisorbed oxygen species ($O_{ads}$), respectively.[35] The presence of the $O_{ads}$ peaks is typically closely associated with surface oxygen vacancies. Due to their reactivity, oxygen vacancies are rapidly oxidized under ambient conditions, leading to the presence of the $O_{ads}$ peak.[36] $O_{ads}$ is observed in pristine BFO due to oxygen vacancy formation during the synthesis process. Vacuum treatment further increases the surface oxygen vacancy concentration at the v-BFO surface, hence the $O_{ads}$ peak is slightly stronger for the v-BFO sample.[37] Unlike v-BFO, down polarization significantly alters the $O_{ads}$ peak by inducing a slight shift to the lower binding energy (530.9 eV) and increasing its intensity. Based on our earlier study,[11] this enhancement at 531.1 eV arises from the accumulation of physisorbed water on the down-poled surface and the formation of surface lattice hydroxide. The latter is initiated by the negatively-charged surface of down-poled BFO (discussed below), which facilitates proton ($H^+$) adsorption from the electrolyte. This process converts surface lattice O to OH, resulting in a new O 1s XPS signal that overlaps with the

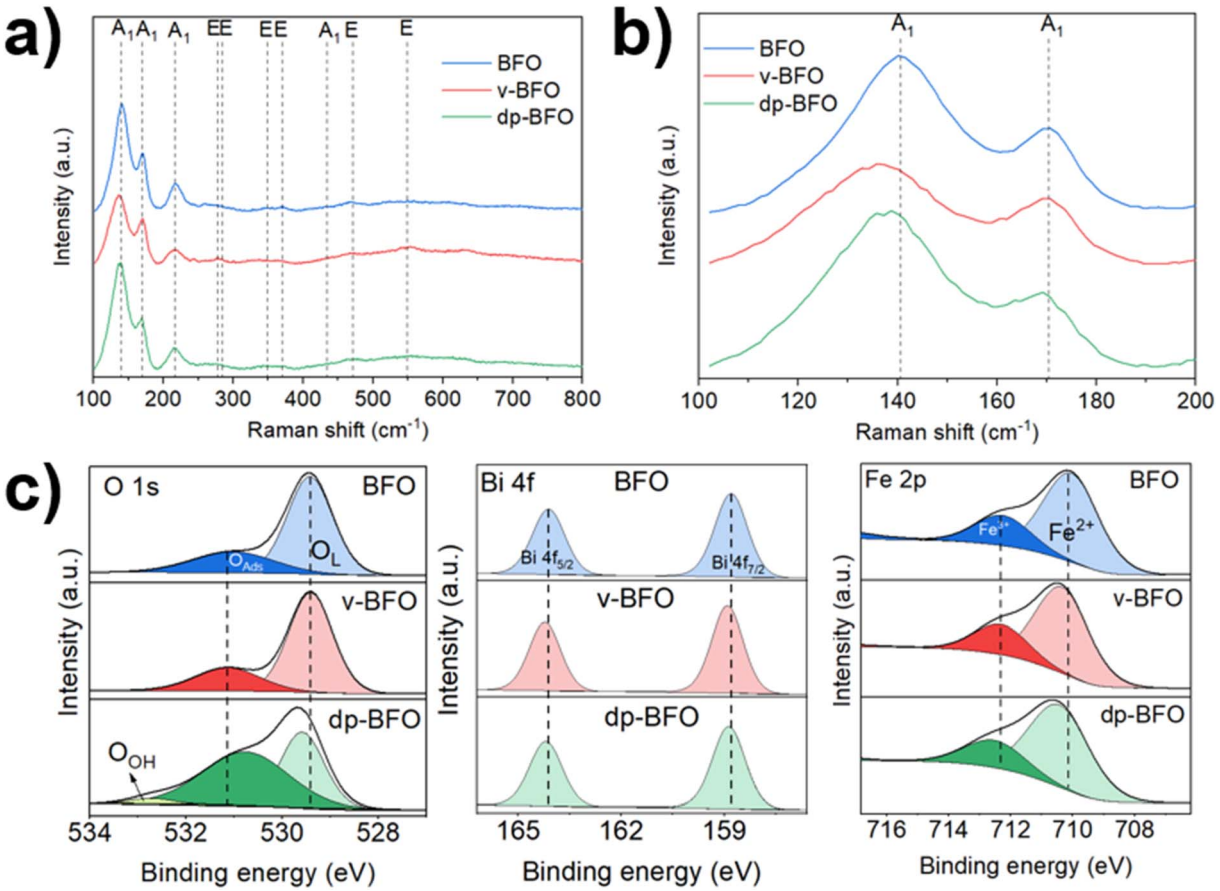


Fig. 3 (a) Raman spectra and (b) magnified Raman spectra in the region 100 – 200 $cm^{-1}$ for the pristine BFO, v-BFO, and dp-BFO thin films. (c) O 1s, Bi 4f and Fe 2p XPS spectra of pristine BFO, v-BFO, and dp-BFO.

$O_{ads}$ peak.[11] Notably, dp-BFO also exhibits an additional peak at 532.9 eV, which is absent in v-BFO. This peak is attributed to chemisorbed water molecules ($O_{W-C}$), as previously identified.[11,38] The formation of surface lattice hydroxide and the accumulation of adsorbed water on the dp-BFO surface synergistically enhance OER by facilitating proton-coupled electron transfer steps and accelerating interfacial charge transfer kinetics.[39]

All samples show Bi 4f peaks at 158.8 and 164.1 eV, corresponding to $Bi^{3+}$.[40] These peaks are found to be slightly shifted towards higher energies (158.9 and 164.2 eV) for both dp-BFO and v-BFO compared with pristine BFO, but no new peaks appear, indicating there is no change in the Bi oxidation state. Pristine BFO exhibits features corresponding to $Fe^{2+}$ at 710.1 eV and $Fe^{3+}$ at 712.4 eV. The presence of these two oxidation states is expected for pristine BFO, attributed to the formation of intrinsic defects such as oxygen and bismuth vacancies during the synthesis.[37] The same two peaks are seen for v-BFO and dp-BFO, but the ratio of $Fe^{3+}$ to $Fe^{2+}$ decreases, to 0.34 for v-BFO and 0.33 for dp-BFO, compared to the pristine BFO (0.35). The decrease in the $Fe^{3+}$ : $Fe^{2+}$ ratio is associated with both the negatively-charged surface and presence of surface oxygen vacancies for dp-BFO surface and with the presence of vacuum-induced oxygen vacancies on the v-BFO. Additionally, following the same trend as the Bi peaks, the Fe peaks for dp-BFO and v-BFO appear at higher energies compared with pristine BFO. The binding energy shifts for bismuth and iron in v-BFO and dp-BFO can be generally attributed to oxygen vacancy formation which would increase the electron density at the cation sites and subsequently increase the binding energies.[16,17]

To gain insights into the local structure of pristine BFO, dp-BFO and v-BFO, X-ray absorption spectroscopy (XAS) was conducted at the Bi $L_{III}$-edge and Fe K-edge. The bulk oxidation state of Bi in the pristine BFO, v-BFO and dp-BFO was determined by comparing the Bi $L_{III}$ X-ray absorption near edge structure (XANES) spectra with the spectrum of a $Bi_2O_3$ reference (Fig. 4a). The Bi $L_{III}$-edge XANES region of the X-ray absorption spectra for all samples overlaps with that of $Bi_2O_3$. The result confirms the existence of $Bi^{3+}$ in BFO and that neither vacuum treatment nor down poling alter the Bi oxidation state, consistent with the XPS results.

The Fe K-edge XANES spectra of the BFO photoelectrodes are compared with that of Fe foil, FeO and $Fe_2O_3$ references (Fig. 4b). The EXAFS fitting parameters are available in Table S2. The spectrum of the pristine BFO overlaps with the $Fe_2O_3$ reference at an edge energy position of 7123.7 eV, indicating that the Fe in bulk BFO is predominantly $Fe^{3+}$. As XAS is a bulk characterization technique while XPS is sensitive only to the

 

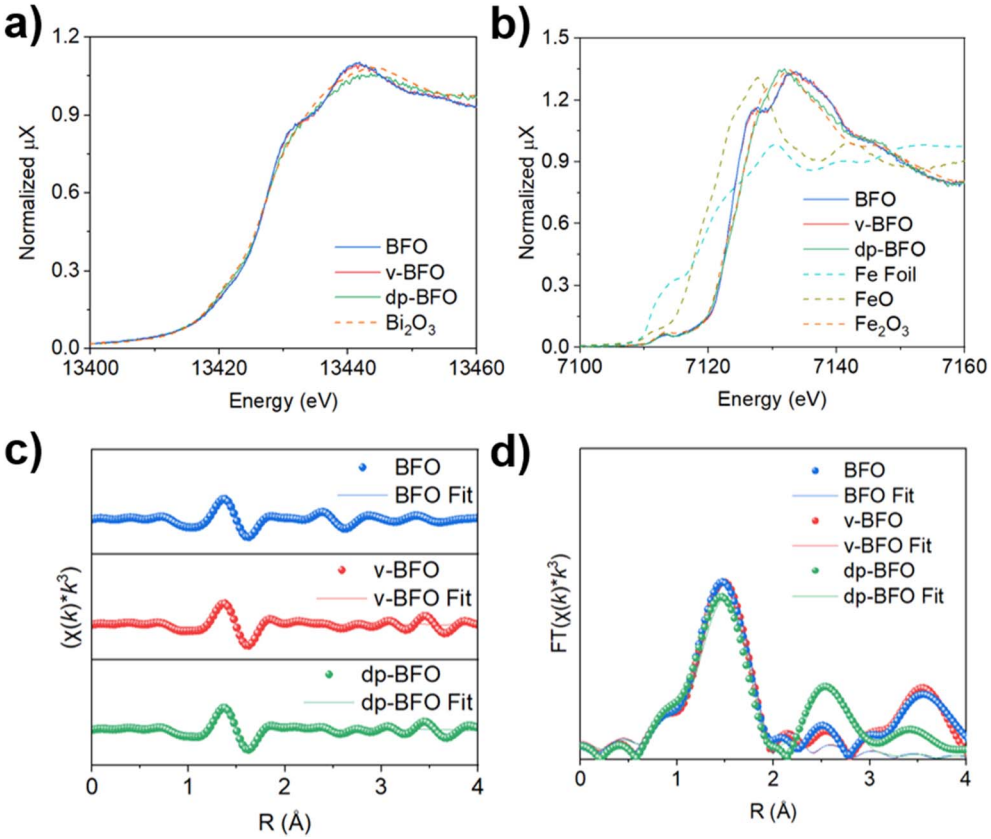


Fig. 4 The X-ray absorption near edge structure (XANES) region of the X-ray absorption spectra of (a) $Bi_2O_3$, BFO, v-BFO and dp-BFO recorded at the Bi $L_{III}$-edge; and (b) Fe foil, FeO, $Fe_2O_3$, BFO, v-BFO and dp-BFO recorded at the Fe K-edge. $\mu X$ is the X-ray absorption. (c) Fit of the $k^3\chi(k)$ EXAFS of BFO, v-BFO and dp-BFO at the Fe K-edge. Fitting range: $2.6 \leq k$ (Å$^{-1}$) $\leq 10$. (d) Fit of the FT of the $k^3\chi(k)$ of BFO, v-BFO and dp-BFO at the Fe K-edge. Fitting range: $1 \leq R$ (Å) $\leq 3$.

surface region (depth of <10 nm), it can be concluded that the $Fe^{2+}$ observed from XPS corresponds to the surface Fe species. As previously mentioned, surficial $Fe^{2+}$ formation is due to bismuth loss and oxygen vacancy formation during the synthesis process.[41] The extended X-ray absorption fine structure (EXAFS) and associated Fourier transform (FT EXAFS) were fitted to extract further local structural information around the $Fe^{3+}$ (Fig. 4c and d). The first coordination shell around the Fe in pristine BFO is well fitted by the Fe–O path with a coordination number of 5.7 and a bond length of 1.98 Å. The Fe K-edge XANES spectrum of v-BFO shares identical features with that of pristine BFO, suggesting the Fe oxidation state in the bulk v-BFO structure is not affected by vacuum treatment.

Conversely, the Fe K-edge XANES spectrum of dp-BFO indicates changes to the local structure upon polarization. While the edge energy position of dp-BFO is the same as for pristine BFO, the shoulder peak at 7127 eV has disappeared. Simultaneously, the post-edge peak at 7133 eV has shifted to a lower energy with a higher white line intensity than the pristine BFO. The peak at 7127 eV is associated with the O 2p band transfer to the Fe 3d orbital, the so-called ligand-to-metal charge transfer process, while the peak at 7133 eV is caused by the 1s to 4p dipole-allowed transition.[42] The fitting results for the EXAFS and FT-EXAFS spectra for dp-BFO at the Fe K-edge further confirm the increase in Fe–O bond length (by 0.01 Å to 1.99 Å) and the decreased Fe–O coordination number (5.3). Based on previous reports, the increase in Fe–O bond length and the decrease in coordination number are indicative of a change to the lattice oxygen in the material.[19,43,44] In contrast to the v-BFO that experiences surface changes alone, the results highlight that the changes to dp-BFO are substantial, affecting the overall bulk structure.

### 3.4 Electronic and optical characteristics

To understand the effect vacuum and down-poling treatments have on the electronic properties of the BFO photoelectrodes, DFT calculations were used to extract information on the electronic densities of states for each sample (Fig. 5a). Based on the characterization outcomes for the v-BFO, the v-BFO was modeled by introducing oxygen vacancies at the upward polarized BFO surface. The Fermi level of v-BFO was calculated to have shifted by 1.2 eV to higher energies (towards the CB) compared to the pristine upward polarized BFO, due to the introduction of occupied, localized mid-gap states above the VB. The ultraviolet photoelectron spectroscopy (UPS, Fig. 5b) result shows the same trend with a 0.2 eV Fermi level shift closer to the CB for v-BFO compared to pristine BFO. Note that the difference in the magnitude of the Fermi level shift arises from the

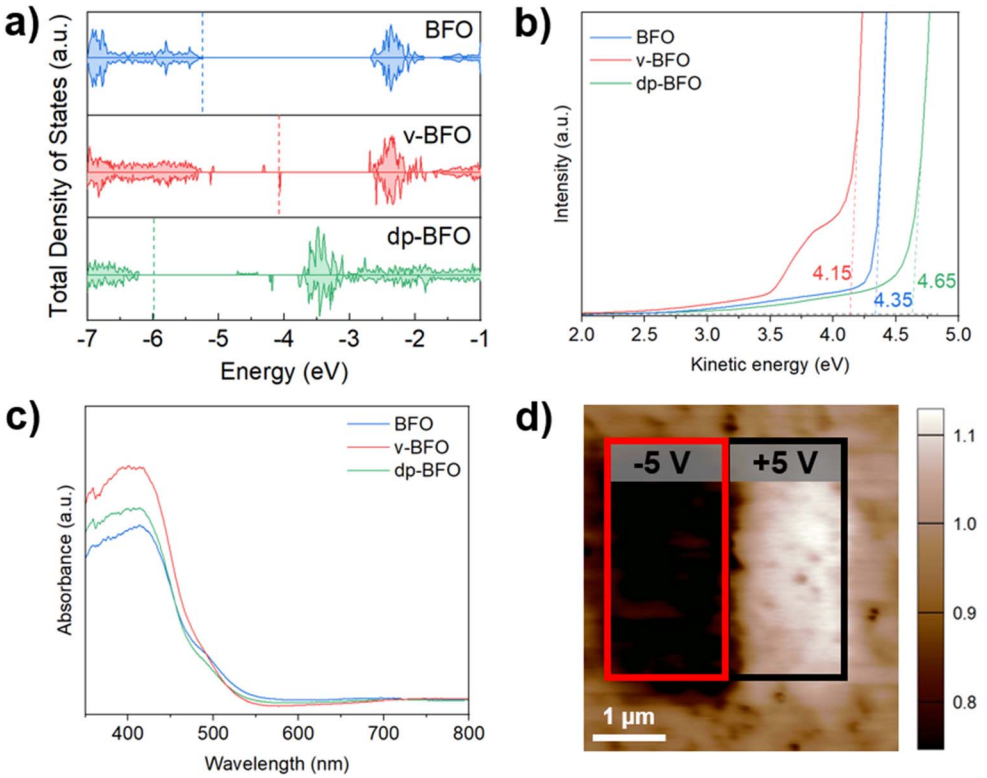


Fig. 5 (a) Total densities of states (DOS) for pristine BFO, v-BFO and dp-BFO as obtained from density functional theory calculations. The dashed lines represent the Fermi level positions. (b) UPS spectra of the pristine BFO, v-BFO and dp-BFO thin films. (c) UV-vis absorbance spectra of the pristine BFO, v-BFO and dp-BFO samples. (d) KPFM CPD profile of the BFO thin film upon ±5 V DC switching. The color scale is in units of Volts.

idealization of the DFT models. The BFO was modeled as a pristine framework possessing no structural defects, whereas the synthesized BFO sample contains inherent oxygen vacancies, as illustrated by the earlier O 1s XPS profile (Fig. 3c). It has been widely reported that oxygen vacancies on the surface of BFO can generate unpaired electrons, and consequently shift the Fermi level to a higher energy (towards the CB).[36,45] Thus, the increased vacancy concentration in v-BFO results in the observed up-shift of the Fermi level towards the CB, with a corresponding increase in electron carrier density and a decrease in hole carrier density. The shift in Fermi level and change in carrier densities leads to a shift from p-type to more n-type behavior. A shift in the Fermi level to a higher energy also impacts the band-bending at the SEI, inducing upward band-bending, facilitating hole transport to the photoelectrode surface which is favorable for the OER.[46] The phenomenon leads to an increased anodic photocurrent density for the v-BFO photoelectrode as more holes can reach the v-BFO surface to oxidize water molecules. Introducing surficial oxygen vacancies has also been reported to facilitate enhanced charge transfer at the SEI in a metal oxide photoanode, and accelerate water oxidation reactions at the surface of photoanodes.[47] The DFT calculations show that the VB and CB positions of v-BFO remain unchanged relative to the original pristine BFO positions, while the UV-vis spectra (Fig. 5c) similarly show no significant change in the band gap.

In contrast, DFT calculations indicated the Fermi level of dp-BFO shifted by 0.8 eV to a lower energy level compared to pristine BFO (Fig. 5a). Similarly, the UPS (Fig. 5b) shows that the Fermi level of dp-BFO shifted by 0.3 eV to a lower energy level. In contrast to v-BFO, the Fermi level shift for dp-BFO theoretically induces stronger downward band bending at the SEI compared to the unpoled BFO, hindering hole transfer to the SEI. As well as the Fermi level shift, the DFT calculations revealed the dp-BFO CB and VB shifted by ~0.9 eV to lower energies compared to the pristine BFO. These calculated band shifts agree with experimentally-obtained VB energies reported in an earlier study.[11] The repositioned VB leads to a greater difference between the VB potential and the electrolyte oxidation potential, which benefits the OER reaction – the larger VB offset creates a wider depletion region and stronger electric fields at the SEI which accelerates the transfer of holes to the dp-BFO surface.[48,49] Further, it has been reported that the electric field across the BFO arising from down polarization induces a gradient in the band energies, promoting hole transport to the SEI.[50–52] Regardless of the band position changes in dp-BFO, the UV-vis spectra (Fig. 5c) and the DFT calculations (Fig. 5a) both show there is no significant change in the band gap.

Measurement of the contact potential difference (CPD) by Kelvin piezoresponse force microscopy (KPFM, Fig. 5d) showed that down poling induces a negatively-charged BFO surface (~250 mV). The change in surface charge will also influence the energy level at the SEI. The negative charge on the dp-BFO

 

surface will invoke upward band bending and facilitate hole transfer at the SEI, which is consistent with the work reported by Li and co-workers.[6] In combination, it appears that the effects of a charged surface, VB shift and gradient modulation for dp-BFO overshadow the downward band bending effect arising from the Fermi level shift. Consequently, the anodic photocurrent density is enhanced under a positive applied potential.

Schematics depicting the distinct influence the BFO treatments have on the charge transfer mechanisms for pristine BFO, v-BFO and dp-BFO, as derived from the findings, are presented in Fig. 6. For pristine BFO, the relatively low Fermi level produces upward band bending at the SEI, which is favorable for electron transfer to the electrolyte but not hole transfer; thus, pristine BFO shows a strong cathodic photocurrent but small anodic photocurrent. In the case of v-BFO, the shifted Fermi level arising from vacuum treatment promotes a shift in band bending at the SEI from upward to downward, accelerating hole transfer to the BFO surface/SEI to drive the OER reaction. The proposed mechanism is supported by PEIS measurement at positive applied potential, which showed a reduced charge transfer resistance at the SEI, corresponding to the increased anodic and decreased cathodic photocurrent for v-BFO relative to pristine BFO. Based on the spectroscopy results showing changes only in the surface chemical and electronic structure, it can be concluded that for v-BFO, the enhanced charge carrier dynamics predominantly occur at the SEI, while the bulk charge transfer behavior remains unchanged compared to pristine BFO. In the case of dp-BFO, the shifted Fermi level delivers stronger downward band-bending at the SEI. However, this effect is overshadowed by: (i) the negatively-charged dp-BFO surface inducing upward band-bending at the SEI; (ii) accelerated hole transfer due to a wider depletion region at the SEI; (iii) band gradient modulation throughout the BFO that facilitates hole transfer to the SEI; and (iv) the formation of surface lattice hydroxide and the accumulation of adsorbed water on the that can accelerate OER. Moreover, the effects unite to improve bulk transport of holes within the BFO towards the SEI (and electrons to the FTO substrate) as well as hole transfer at the SEI, confirmed by the reduced charge transfer resistance seen from PEIS and evidence from spectroscopy of changes in both the bulk and surface structure, which accounts for the improved anodic PEC performance, with negligible cathodic photocurrent production.

The oxygen vacancies in v-BFO affect the charge dynamics predominantly at the SEI. Consequently, it is expected that v-BFO will exhibit n-type behavior only when it is thin enough for the surface effects to be dominant and govern photoelectrode behavior. In a thicker photoelectrode, the impact of vacuum annealing will not be as significant with the subdued effect not sufficient to control the semiconducting behavior.

To validate this hypothesis, both vacuum annealing and downward poling were applied to BFO films of two additional thicknesses (65 nm and 260 nm), with film thickness tuned by varying the number of deposition cycles while keeping all other parameters constant to minimize extraneous influences. Given that surface roughness can affect both ferroelectric poling behavior and PEC performance, atomic force microscopy (AFM) measurements were conducted for all BFO films.[53] The results (Table S3, SI) confirmed similar surface roughness values for the 65 nm, 135 nm, and 260 nm films, suggesting that surface roughness plays a negligible role in modulating polarization or PEC activity. All BFO films were poled using a fixed bias of −8 V, which is sufficient for full polarization switching across the different film thicknesses, based on the known coercive field of BFO (150–370 kV $cm^{-1}$) and the observed phase switching in PFM measurements (Fig. S6).[54,55]

For the 65 nm-thick BFO photoelectrode (Fig. S5a and b), the impact of vacuum annealing on anodic photocurrent density is more significant than for a 260 nm-thick BFO layer (Fig. S5c and d). Notably, the performance enhancement of the 135 nm film

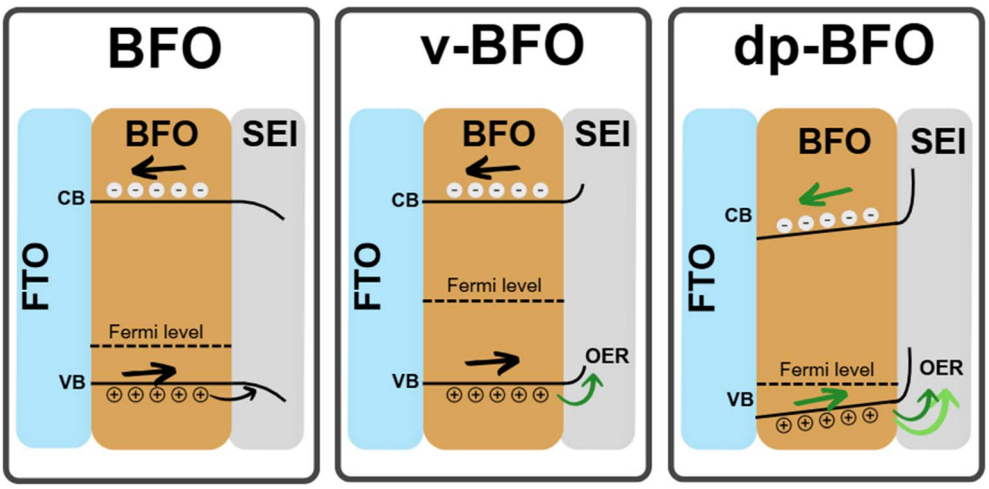


Fig. 6 Schematics depicting the charge transfer mechanisms in pristine BFO, v-BFO and dp-BFO photoanodes at an applied positive bias. The impact on charge transport of SEI band bending, electronic band shifting and gradients in band energies within the BFO layer, arising from the vacuum annealing and down poling treatments, are illustrated. Arrow colors indicate the relative rates of charge transfer: The green arrows in v-BFO and dp-BFO represent faster charge transfer relative to the black arrows in pristine BFO.

lies between that of the 65 nm and 260 nm samples. In contrast, the PEC enhancement achieved by downward polarization remained consistent across all film thicknesses, indicating that the polarization effect extends beyond charge transfer dynamics at the SEI as well as across the bulk structure. This demonstrates that downward poling enhances anodic PEC performance in a thickness-independent manner.

## 4 Conclusions

Ferroelectric polarization has been demonstrated to manipulate the behavior of pristine BFO for PEC reduction or oxidation reactions. The internal electrical field in BFO enables regulation of the n/p-type behavior of the material by exploiting its switchable polarization capacity. Down-poling a BFO thin film yields better anodic performance than the conventional vacuum-annealing of BFO thin film. Vacuum annealing introduces surfice oxygen vacancies and shifts the Fermi level towards the CB with charge transfer efficiency improved at the SEI. In contrast, while down-poling shifts the Fermi level to a lower energy (more positive potential), it also enhances both bulk and interfacial charge transfer within the BFO film. These improvements arise from a combination of effects from the negatively-charged surface, negatively shifted band energies, positive energy gradient, the formation of surface lattice hydroxide and accumulation of chemisorbed water on the dp-BFO. Together, these factors outweigh the Fermi level shift and facilitate photo-generated hole transfer, thereby, intensifying photoanodic performance. The findings highlight the significant potential of ferroelectric polarization to readily and rapidly alter the p/n behavior of a photoelectrode under mild treatment conditions.

## Author contributions

M. Gunawan: Conceptualization, methodology, investigation, formal analysis, writing – original draft preparation. Y. Jin: Investigation, formal analysis, writing – original draft preparation. T.C. Leung: Investigation, formal analysis. O. Bowdler: Formal analysis, methodology, validation. S. Zhou: Methodology, writing – reviewing & editing. D. Gunawan: Formal analysis, investigation, validation. M. Zhang: Formal analysis. X. Fang: Formal analysis, Q. Zhang: Methodology, validation, writing – reviewing & editing. N. Valanoor: Conceptualization, supervision, resources, funding acquisition, writing – reviewing & editing. R. Amal: Supervision, conceptualization, resources, funding acquisition, writing – reviewing & editing. J. N. Hart: Supervision, conceptualization, resources, funding acquisition, writing – reviewing & editing. J. Scott: Supervision, conceptualization, resources, funding acquisition, writing – reviewing & editing. C. Y. Toe: Supervision, conceptualization, methodology, funding acquisition, writing – reviewing & editing.

## Conflicts of interest

There are no conflicts to declare.

## Data availability

The data supporting this article have been included as part of the SI, including EXAFS & EIS fitting parameters, supplementary characterizations such as XRD, PFM, SEM, surface roughness measurement and supplementary PEC performance data. See DOI: https://doi.org/10.1039/d5ta04859a.

## Acknowledgements

The authors acknowledge the facilities and the scientific and technical assistance of Microscopy Australia at the Electron Microscope Unit (EMU) and other characterization facilities within the Mark Wainwright Analytical Centre (MWAC) at UNSW Sydney. The computational resources necessary for the research were made available by the Australian Government through the National Computational Infrastructure (NCI) under the National Computational Merit Allocation Scheme. XAS analysis was undertaken in part using the MEX-1 beamline at the Australian Synchrotron, part of ANSTO (AS241/MEX1/21367). The authors thank Dr Rosalie Hocking and Dr Emily Finch for their support and assistance with the XAS measurements. The work was supported by the Australian Research Council (ARC) through a Discovery Project (DP210102694), the Training Centre for the Global Hydrogen Economy (IC200100023), and the Centre of Excellence in Future Low-Energy Electronics Technologies (CE170100039). Q.Z. acknowledges support from the CSIRO Quantum Technologies Future Science Platform and IWY program grant and a Women in FLEET Fellowship.

## References

1 T. Faunce, S. Styring, M. R. Wasielewski, G. W. Brudvig, A. W. Rutherford, J. Messinger, A. F. Lee, C. L. Hill, H. Degroot, M. Fontecave, D. R. MacFarlane, B. Hankamer, D. G. Nocera, D. M. Tiede, H. Dau, W. Hillier, L. Wang and R. Amal, *Energy Environ. Sci.*, 2013, **6**, 1074–1076.
2 C. Y. Toe, S. Zhou, M. Gunawan, X. Lu, Y. H. Ng and R. Amal, *J. Mater. Chem. A*, 2021, **9**, 20277–20319.
3 S. Y. Jeong, J. Song and S. Lee, *Appl. Sci.*, 2018, **8**, 1388.
4 J. Silva, A. Reyes, H. Esparza, H. Camacho and L. Fuentes, *Integr. Ferroelectr.*, 2011, **126**, 47–59.
5 Y.-L. Huang, W. S. Chang, C. N. Van, H.-J. Liu, K.-A. Tsai, J.-W. Chen, H.-H. Kuo, W.-Y. Tzeng, Y.-C. Chen, C.-L. Wu, C.-W. Luo, Y.-J. Hsu and Y.-H. Chu, *Nanoscale*, 2016, **8**, 15795–15801.
6 X. Li, Z. Wang, W. Ji, T. Lu, J. You, K. Wang, G. Liu, Y. Liu and L. Wang, *ACS Nano*, 2023, **17**, 22944–22951.
7 Q. Jing, Z. Liu, X. Cheng, C. Li, P. Ren, K. Guo, H. Yue, B. Xie, T. Li, Z. Wang and L. Shu, *Chem. Eng. J.*, 2023, **464**, 142617.
8 M. Gunawan, S. Zhou, D. Gunawan, Q. Zhang, J. N. Hart, R. Amal, J. Scott, N. Valanoor and C. Y. Toe, *J. Mater. Chem. A*, 2025, **13**, 1612–1640.
9 D. Cao, Z. Wang, Nasori, L. Wen, Y. Mi and Y. Lei, *Angew. Chem., Int. Ed.*, 2014, **53**, 11027–11031.

 

10 A. Kakekhani and S. Ismail-Beigi, *ACS Catal.*, 2015, **5**, 4537–4545.
11 M. Gunawan, O. Bowdler, S. Zhou, X. Fang, Q. Zhang, Y. Sakamoto, K. Sun, D. Gunawan, S. L. Y. Chang, R. Amal, N. Valanoor, J. Scott, J. N. Hart and C. Y. Toe, *Adv. Funct. Mater.*, 2025, **35**, 2417651.
12 O. V. Nkwachukwu, C. Muzenda, K. D. Jayeola, T. I. Sebokolodi, D. S. Sipuka, H. Wu, B. A. Koiki, M. Zhou and O. A. Arotiba, *Electrochim. Acta*, 2023, **454**, 142385.
13 N. P. Prasad, M. Rohnke, M. A. Verheijen, J. M. Sturm, J. P. Hofmann, E. J. M. Hensen and A. Bieberle-Hütter, *ACS Appl. Energy Mater.*, 2023, **6**, 12237–12248.
14 S. Das, P. Fourmont, D. Benetti, S. G. Cloutier, R. Nechache, Z. M. Wang and F. Rosei, *J. Chem. Phys.*, 2020, **153**, 084705.
15 A. Radmilovic, T. J. Smart, Y. Ping and K.-S. Choi, *Chem. Mater.*, 2020, **32**, 3262–3270.
16 D. Chen, F. Niu, L. Qin, S. Wang, N. Zhang and Y. Huang, *Sol. Energy Mater. Sol. Cells*, 2017, **171**, 24–32.
17 S. Wang, D. Chen, F. Niu, N. Zhang, L. Qin and Y. Huang, *J. Alloys Compd.*, 2016, **688**, 399–406.
18 J. Song, T. L. Kim, J. Lee, S. Y. Cho, J. Cha, S. Y. Jeong, H. An, W. S. Kim, Y.-S. Jung, J. Park, G. Y. Jung, D.-Y. Kim, J. Y. Jo, S. D. Bu, H. W. Jang and S. Lee, *Nano Res.*, 2018, **11**, 642–655.
19 Y. Tian, A. Wang, Y. Wei, M. Pei, R. Cao, Z. Gu, Q. Yuan, Y. Hu, J. Wang, K. Liu, D. Shang, J. Niu, X. An, R. Long and J. Zhang, *Adv. Funct. Mater.*, 2022, **32**, 2111180.
20 Q. Zhang, N. Valanoor and O. Standard, *J. Mater. Chem. C*, 2015, **3**, 582.
21 A. Erba, J. K. Desmarais, S. Casassa, B. Civalleri, L. Donà, I. J. Bush, B. Searle, L. Maschio, L.-E. Daga, A. Cossard, C. Ribaldone, E. Ascrizzi, N. L. Marana, J.-P. Flament and B. Kirtman, *J. Chem. Theory Comput.*, 2023, **19**, 6891–6932.
22 D. Becke, *J. Chem. Phys.*, 1993, **98**, 5648–5652.
23 C. Lee, W. Yang and R. G. Parr, *Phys. Rev. B:Condens. Matter Mater. Phys.*, 1988, **37**, 785.
24 H. Vosko, L. Wilk and M. Nusair, *Can. J. Phys.*, 1980, **58**, 1200–1211.
25 J. Stephens, F. J. Devlin, C. F. Chabalowski and M. J. Frisch, *J. Phys. Chem.*, 1994, **98**, 11623–11627.
26 S. Grimme, J. Antony, S. Ehrlich and H. Krieg, *J. Chem. Phys.*, 2010, **132**, 154104.
27 S. Grimme, S. Ehrlich and L. Goerigk, *J. Comput. Chem.*, 2011, **32**, 1456–1465.
28 S. Grimme, A. Hansen, J. G. Brandenburg and C. Bannwarth, *Chem. Rev.*, 2016, **116**, 5105–5154.
29 S. Zhou, K. Sun, C. Y. Toe, J. Huang, A. Wang, J. Yuwono, P. Kumar, T. Wan, D. Zhang, Z. Ma, J. Vongsvivut, D. Chu, X. Hao and R. Amal, *Appl. Catal., B*, 2024, **348**, 123836.
30 C. Zhang, Y. Li, M. Chu, N. Rong, P. Xiao and Y. Zhang, *RSC Adv.*, 2016, **6**, 24760.
31 T. Yang, J. Wei, Y. Guo, Z. Lv, Z. Xu and Z. Cheng, *ACS Appl. Mater. Interfaces*, 2019, **11**, 23372–23381.
32 Y. Ma, W. Xing, J. Chen, Y. Bai, S. Zhao and H. Zhang, *Appl. Phys. A:Mater. Sci. Process.*, 2016, **122**, 63.
33 J. Wei, C. Wu, Y. Liu, Y. Guo, T. Yang, D. Wang, Z. Xu and R. Haumont, *Inorg. Chem.*, 2017, **56**, 8964–8974.
34 A. Lahmar, K. Zhao, S. Habouti, M. Dietze, C.-H. Solterbeck and M. Es-Souni, *Solid State Ionics*, 2011, **202**, 1–5.
35 S. Wang, P. Chen, J.-H. Yun, Y. Hu and L. Wang, *Angew. Chem., Int. Ed.*, 2017, **56**, 8500–8504.
36 Z. Wang, R. Lin, Y. Huo, H. Li and L. Wang, *Adv. Funct. Mater.*, 2022, **32**, 2109503.
37 N. Dix, R. Muralidharan, B. Warot-Fonrose, M. Varela, F. Sánchez and J. Fontcuberta, *Chem. Mater.*, 2009, **21**, 1375–1380.
38 X. Chen, C. Liu, Z. Hua and N. Ma, *ACS Appl. Mater. Interfaces*, 2022, **14**, 49965–49974.
39 A. Sengeni and V. Aravindan, *Adv. Energy Mater.*, 2020, **10**, 1902666.
40 M. Tayebi, A. Tayyebi, T. Soltani and B.-K. Lee, *New J. Chem.*, 2019, **43**, 9106–9115.
41 A. Manzoor, A. M. Afzal, M. Umair, A. Ali, M. Rizwan and M. Z. Yaqoob, *J. Magn. Magn. Mater.*, 2015, **393**, 269–272.
42 T. Gholam, L. R. Zheng, J. O. Wang, H. J. Qian, R. Wu and H.-Q. Wang, *Nano Express*, 2019, **14**, 137.
43 Y. Gao, M. Zhang, Y. Jin, M. Zhou, Y. Mao, J. Sun, W. Wang and Z. Song, *Appl. Catal., B*, 2024, **341**, 123348.
44 M. Li, J. Deng, A. Pu, P. Zhang, H. Zhang, J. Gao, Y. Hao, J. Zhong and X. Sun, *J. Mater. Chem. A*, 2014, **2**, 6727–6733.
45 L. Hao, H. Huang, Y. Zhang and T. Ma, *Adv. Funct. Mater.*, 2021, **31**, 2100919.
46 C. Jiang, S. J. A. Moniz, A. Wang, T. Zhang and J. Tang, *Chem. Soc. Rev.*, 2017, **46**, 4645.
47 L. Yan, G. Dong, X. Huang, Y. Zhang and Y. Bi, *Appl. Catal., B*, 2024, **345**, 123682.
48 F. E. Osterloh, *Chem. Mater.*, 2008, **20**, 35–54.
49 A. Kudo and Y. Miseki, *Chem. Soc. Rev.*, 2009, **38**, 253–278.
50 J. Xie, C. Guo, P. Yang, X. Wang, D. Liu and C. M. Li, *Nano Energy*, 2017, **31**, 28–36.
51 T. Lv, J. Li, N. Arif, L. Qi, J. Lu, Z. Ye and Y.-J. Zeng, *Matter*, 2022, **5**, 2685–2721.
52 K. Wang, C. Han, J. Li, J. Qiu, J. Sunarso and S. Liu, *Angew. Chem., Int. Ed.*, 2021, **61**, e202110429.
53 J. Wang, G. Liu, D. Sando, N. Valanoor and J. Seidel, *Appl. Phys. Lett.*, 2017, **111**, 092902.
54 M. Zhu, H. Zheng, J. Zhang, G. Yuan, K. Wang, G. Yue, F. Li, Y. Chen, M. Wu and W. Zhang, *Appl. Phys. Lett.*, 2017, **111**, 032901.
55 J. H. Shah, H. Ye, Y. Liu, A. M. Idris, A. S. Malik, Y. Zhang, H. Han and C. Li, *J. Mater. Chem. A*, 2020, **8**, 6863–6873.